Bull Eng Geol Environ
DOI 10.1007/s10064-012-0416-9

ORIGINAL PAPER

Can weathering improve the toughness of a fractured rock? A case study using the San Giacomo granite

Stefano Cuccuru · Leonardo Casini · Giacomo Oggiano · Gian Piero Cherchi

Received: 20 April 2011 / Accepted: 12 February 2012

Abstract The physical–mechanical behaviour of the weathered San Giacomo granite, Sardinia, has been investigated using a combination of physical–mechanical tests and microstructural analysis. Fieldwork and microscopy suggest a pervasive microfracture system developed on a pre-existing magmatic quartz anisotropy. Alteration indices, chemical analyses and mineralogy indicate that the yellow staining is produced by the circulation of oxygen-rich rainwater through microfractures in the rock, resulting in the oxidation of biotites. Apart from the obvious modification of the original grey colouring, the precipitation of Fe-oxides and hydroxides has welded fractures together, leading to the partial recovery of the physical–mechanical properties previously compromised due to microfracturing.

Keywords Weathering · Microfractures · Quartz LPO · Granite · Corsica–Sardinia Batholith

Résumé Le comportement physico-mécanique du granite altéré de San Giacomo (Sardaigne) a été étudié à partir de plusieurs essais physico-mécaniques et des analyses microstructurales. Les observations de terrain et au microscope suggèrent qu'un système généralisé de microfractures s'est développé à partir d'une anisotropie préexistante des quartz d'origine magmatique. Des indices d'altération, des analyses chimiques et minéralogiques indiquent que la coloration jaune est produite par la circulation d'eaux de pluie, riches en oxygène, au travers des micro-fractures de la roche, avec pour conséquence l'oxydation des biotites. En dehors de la modification évidente de la couleur grise d'origine, les précipitations d'oxydes et d'hydroxydes de fer ont soudé ensemble les fractures, conduisant à une récupération partielle des propriétés physico-mécaniques qui avaient été affaiblies par la micro-fracturation.

Mots clés Altération météorique · Quarts LPO · Granite · Corse-Sardaigne Batholite · Microfractures

Introduction

Variscan granites in the Corsica–Sardinia Batholith (CSB) of northern Sardinia (Italy) represent an important resource. In addition to limited quarrying in the Roman Imperial age, extensive exploitation of granitic rocks in the La Maddalena archipelago began in the second half of the nineteenth century when technological advances enabled the winning of large, homogeneous blocks of granite (Aversano 2003). At present, several varieties of granites are quarried according to their physical properties, including colour and texture (Cherchi 2005). These rocks have a porphyritic texture and a visible fabric as a result of the shape-preferred orientation (SPO) of pinkish K-feldspar megacrysts, micro-granular mafic aggregates, and biotite schlieren (Cherchi 2005). Such a texture primarily results from late-stage flow in the crystal "mush" when the crystal load increases in the rising melt (Paterson et al. 1989). On a micro-scale, late-stage magmatic hydrothermal flow (HT) is further evidenced by the lattice-preferred orientation (LPO) of quartz and by the occurrence of melt pockets with healed fractures in the feldspar megacrysts.

S. Cuccuru (✉) · L. Casini · G. Oggiano
Dipartimento di Scienze Botaniche, Ecologiche e Geologiche, Università di Sassari, Via Piandanna 4, 07100 Sassari, Italy
e-mail: scuccuru@uniss.it

G. P. Cherchi
A.R.P.A. Dip. Prov. Sassari, Via Rockefeller 58, 07100 Sassari, Italy

Published online: 05 April 2012

The San Giacomo granite (SG-Granite) formed as a result of a late-stage magmatic pulse in the Arzachena Pluton (Oggiano et al. 2005; Casini et al. 2008). Among the granite varieties found in Sardinia, the SG-Granite is perhaps the most valued because of its yellowish colour. Quarrying operations over historical times have attested to a strong load resistance, which is unexpected in weathered granite. The aim of this work was to establish the causes of the yellow staining in the SG-Granite and to investigate the anomalous mechanical behaviour of the rock using an integrated chemical, micro-structural and physical–mechanical approach.

Geological setting

The Arzachena Pluton

Approximately half of the Sardinian Variscan basement consists of granites, forming the southern edge of the huge CSB, which was emplaced during the last stage of the Variscan Orogeny (Carmignani et al. 1994; Matte 2001) at 350–285 Ma (Paquette et al. 2003). After the Variscan cycle, the margins of the Sardinia block experienced minor brittle deformation, localized along strike-slip faults (Oggiano et al. 2009), as a result of deformation within the Alpine belt. The CSB is highly heterogeneous and reflects multiple episodes of intrusion over more than 50 million years during rapid changes in the geodynamic setting (Paquette et al. 2003; Ferrè and Leake 2001). One of the largest intrusions in Sardinia is the composite, metaluminous, Arzachena Pluton (Fig. 1).

Oggiano et al. (2005) distinguished four main magmatic lithofacies, interpreted as progressively younger and more differentiated magmatic pulses (Oggiano et al. 2005; Gaggero et al. 2007). About 60 % of the intrusion consists of inequigranular, medium-grained biotite-monzogranite (lithofacies 2), exploited in some areas and traded as "Rosa Beta" granite. The remaining part is made up of hornblende/biotite-granodiorite (lithofacies 1), coarse-grained biotite-monzogranite (lithofacies 3), and leuco-monzogranite (lithofacies 4). The contacts between different lithofacies are usually gradational and broad, indicating that emplacement of the pluton occurred over a relatively short time-span. This interpretation is supported by the widespread occurrence of mixing/mingling structures, indicating negligible rheological differences among compositionally different units during emplacement. A well-defined magmatic fabric is present throughout the pluton except in leuco-monzogranites which are generally fine-grained and almost isotropic. In the other magmatic units, the flow foliation and lineation are defined by the SPO of pinkish K-feldspar phenocrysts and by mafic

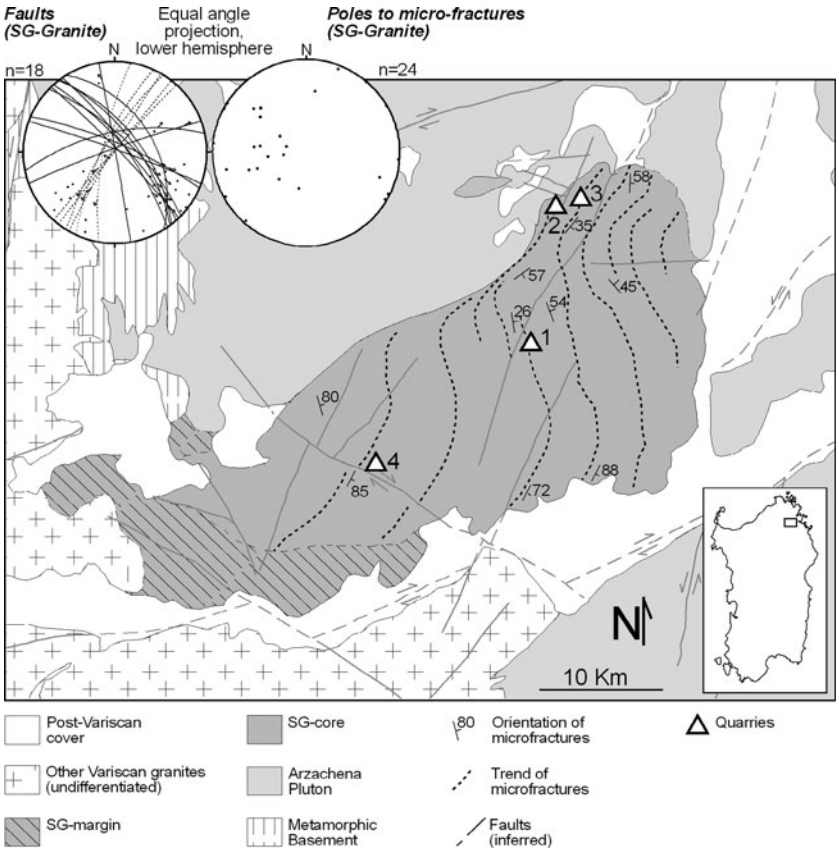

Fig. 1 Structural–geological map of the SG-Granite (see key to the map for explanation). In the *upper left side* are shown the lower hemisphere equal angle projections of the main faults and J1 microfractures

and micro-granite enclaves. The lineation trend is generally NW–SE, and the foliation dips gently to moderately towards the NE. These general trends show large variations in the peripheral part of the intrusion, probably due to local flow perturbation and edge effects.

The San Giacomo (SG)-Granite

The SG-Granite (lithofacies 4) is a medium- to fine-grained leuco-monzogranite containing quartz (42 %), K-feldspar (20 %), microcline (7 %), plagioclase (20 %), and biotite (<5 %). In map-view, the intrusion has an elliptical shape roughly elongated N060, i.e., the magmatic body is largely discordant with respect to the general trend of the host Arzachena Pluton (Fig. 1). Field observations reveal a narrow and discontinuous chilled margin, which is porphyritic and fine-grained (average grain size <1 cm), developed against the migmatites (SG-margin; Fig. 1). Within this porphyritic shell, feldspar phenocrysts define a weak magmatic foliation that is roughly concentric and parallel to the contact itself. This feature, however, is not recognizable outside the margin. Even so, a distinctive microfracture network, roughly parallel to the plane of magmatic foliation, means this fabric can be observed throughout the whole massif. Microfractures must have formed either during or shortly after the granite was emplaced, and are offset by post-Variscan structures such as early Permian and younger faults (Fig. 1). In the core of the leuco-monzogranite (SG-core in Fig. 1), phenocrysts, femic enclaves, and other flow markers tend to be absent, making it difficult to distinguish a clear SPO. These rocks therefore show an apparently homogeneous and quasi-isotropic texture. Towards the middle part of the granitic body, the average grain size increases to 1.5 cm.

A previously proposed emplacement model suggests that leucogranite was squeezed out from the less acid core of the Arzachena Pluton during the final stages of crystallization and cooling, at depths as shallow as 4–5 km (Casini et al. 2008). The Arzachena Pluton and SG-Granite underwent extensive brittle faulting as a result of the tertiary strike-slip tectonics that affected the island during Oligocene–Miocene times (Oggiano et al. 2009). Faulting led to the development of a widely interconnected network of weak, permeable zones, crossing otherwise strong granitic units (Fig. 1).

Methods

Several oriented samples were taken from the exploited yellowish layer in five quarries, using the orientation of the microfracture network as a reference frame (Fig. 2). The deepest quarry (indicated as '1' in Fig. 1) exposes fresh through to progressively weathered material, which was

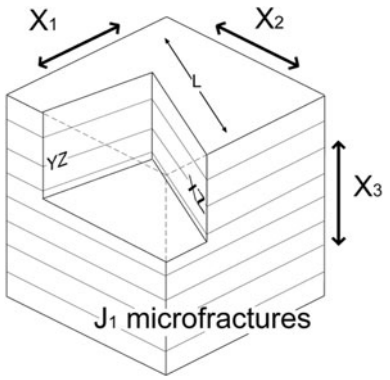

Fig. 2 Sample orientation respect to J1 microfractures (*horizontal*) *L* indicates the inferred magmatic lineation, the *XZ* and *YZ* planes indicates the orientation of thin sections, X_1, X_2 and X_3 indicate the three reference directions selected for the UV test

logged. Two sets of samples were collected from this site, from both fresh (001) and yellowish (040) granite. Flexural strength (FS) tests (UNI 9724/5) were carried out on 54 tablets, 12 × 3 × 2 cm. Other standard characterization tests were performed on 60 cubes (7 × 7 × 7 cm). Dry density, water absorption at atmospheric pressure, open porosity, water absorption capillarity, uniaxial compressive strength (UCS), and FS were measured directly, following the relevant UNI EN protocols (UNI 1990a, b, 1992, 2000a, b, 2002, respectively). Ultrasonic analysis employed the 'direct method' (Kahraman and Yeken 2008) using a CONTROLS E48 ultrasonic pulse velocity tester with two transducers with a frequency of 54 kHz. To reduce noise, samples were positioned on an isolating foam sheet. While taking measurements, transducers were hand-pressed firmly onto the specimens. To ensure good adhesion between the specimen and transducers, the contact surfaces were sprinkled with a hydro-soluble gel. Each direction (X_1, X_2 and X_3) was tested. The plane X_1–X_2 was then made parallel to the macroscopic microfracture (Fig. 2).

Given the macroscopic anisotropy evidenced by microfractures, UCS and capillarity absorption tests were performed with specimens oriented in two mutually orthogonal positions, making the microfractures either parallel or normal to the loading direction or water surface, respectively, according to the test. Further microfractures and the infilling material were studied by polarized optical microscopy and with a scanning electron microscope (SEM; EVO LS10) equipped with an Oxford energy dispersive X-ray detector (EDX), INCA-Xact. Samples for SEM analysis were polished with alumina gel and coated with a thin carbon film (2–4 nm).

Microscopic investigations, including quartz textural analysis and micro-structural observations, were performed on standard-thickness (30 μm) thin sections oriented normal to the microfracture network, both parallel (XZ) and normal (YZ) to the inferred magmatic lineation (Fig. 2).

The microfracture network was characterized using the microfracture density (*Dc*) parameter, which is defined hereafter as the crack number per unit length. Cracks were measured with the linear intercept method (Launeau and Robin 1996; Nasseri et al. 2005; Sousa et al. 2005), with average values obtained from six randomly oriented lines. To fully consider the effective impact of microfractures on rock permeability, another dimensionless parameter for network connectivity (*Cc*) was established, defined as the average number of connections between cracks crossing on the intercept and other cracks. The K value represents the ratio between *Cc* and *Dc*.

Fracture analysis, quartz LPO, and the orientation of sub-grain and grain boundaries of all samples were determined optically using a Leitz laborlux 12 POL microscope equipped with a 5-axis Leitz Universal Stage.

Major element compositions were determined by X-ray fluorescence (XRF) using a Bruker S4 EXPLORER X-ray spectrometer. To investigate chemical variations between the grey (fresh) and yellowish (weathered) portions of the SG-Granite, two sets of samples were analysed for major and trace element composition by ICP–MS at Activation Laboratories Ltd (Ancaster, Ontario, Canada). Finally, the weathering grade was determined using both the qualitative weathering scale proposed by Gupta and Seshagiri (2000) and the quantitative chemical index of alteration (CIA) (Nesbitt and Young 1982), which takes into account the degree of feldspar weathering as a marker of general weathering. This index indicates fresh granites should have a CIA value of 45–55 %.

Results

Whole rock chemistry and weathering grade

XRF analysis indicates minor differences between sample sets (Table 1). Sample 004 is set apart from this trend and shows slightly lower Al_2O_3 and Na_2O contents (<10 and <3 %, respectively). These minor differences may be a result of the sample being derived from the periphery of the SG-Granite sheet, where mixing and hybridization with the less differentiated part of the Arzachena Pluton is expected. Apart from this expected heterogeneity close to the margins, the SG-Granite is compositionally homogeneous with average contents of 0.9 % Fe_2O_3, 0.6 % CaO, 0.05 % MgO, 3.2 % Na_2O, 4.6 % K_2O, and 0.8 % TiO_2. ICP–MS analyses (Tables 2, 3) of grey (001) and yellowish (040) SG-Granite also showed little difference between the samples, with the exception of the state of iron oxidation.

Following the weathering scale proposed by Gupta and Seshagiri (2000), the quarried yellowish SG-Granite can be considered as slightly to moderately weathered. On this scale, the greyish part is less weathered. However, the CIA index, which is a quantitative parameter of the intensity of chemical weathering, does not indicate any difference between the yellowish samples and the unstained, deeper portions of the granite. CIA index values (Table 1) range from 54 to 58 %, which is typical of weakly weathered granite (Nesbitt and Young 1982).

Physical–mechanical properties

The physical–mechanical data (Table 3) show that both microfracturing and weathering have weakened the SG-Granite with respect to other, fresher granites free of brittle

Table 2 Major elements composition

	Samples	
	001	040
SiO_2	76.63	77.59
Al_2O_3	12.63	12.18
Fe_2O_3	0.77	0.78
FeO	0.47	0.29
MnO	0.031	0.02
MgO	0.06	0.05
CaO	0.65	0.57
Na_2O	3.51	3.34
K_2O	4.82	4.74
TiO_2	0.07	0.06
S	0.01	0.01
P_2O_5	0.03	0.03
LOI	0.28	0.28
TOT	99.97	99.95

ICP MS (%)

Table 1 Chemical analyses (XRF) and CIA index

Sample	Al_2O_3 (%)	Fe_2O_3 (%)	CaO (%)	MgO (%)	Na_2O (%)	K_2O (%)	TiO_2 (%)	CIA (%)
001	12.63	0.77	0.65	0.06	3.51	4.82	0.07	58.44
004	9.49	0.99	0.67	0.06	2.66	4.59	0.13	54.51
007	10.22	0.99	0.38	0.01	3.19	4.23	0.05	56.71
023	10.57	1.01	0.74	0.07	3.06	4.54	0.12	55.90
040	12.18	0.78	0.57	0.05	3.34	4.74	0.06	58.47

Table 3 Physical mechanical properties of the SG-Granite

Sample	Dry density (g/cm^3)	Water abs. at atm. pr. (%)	Open porosity (%)	Water absorption capillarity (g/m^2 s$^{0.5}$)			UCS (MPa)			Flexure strength (MPa)			Ultrasonic velocity (m/s)			
				C_1	C_2	Mean	0°	90°	Mean	90°	0°	Mean	X_1	X_2	X_3	Mean
001	2.56	0.52	1.34	1.149	1.096	1.122	102.21	178.06	140.14	14.39	13.83	14.11	3,589.7	4,069.8	3,414.6	3,691.4
004	2.68	0.62	1.64	0.922	0.802	0.862	175.25	197.75	186.5	16.9	18.23	17.56	4,861.1	4,666.7	4,635.8	4,721.2
007	2.76	0.64	1.77	1.824	1.744	1.784	149.49	154.34	151.91	6.08	7.23	6.65	2,800	3,030.3	2,892.6	2,907.6
023	2.59	0.6	1.55	1.373	1.273	1.323	143.88	169.73	156.8	11.81	12.74	12.27	3,043.5	4,191.6	3,286.4	3,507.2
040	2.71	0.59	1.6	1.613	1.619	1.616	169.05	151.02	160.03	13.78	12.52	13.15	3,833.7	3,754.7	3,612.7	3,733.7
Mean	2.66	0.59	1.58	1.38	1.31	1.34	147.98	170.18	159.08	12.59	14.33	12.63	3,625.6	3,942.6	3,568.4	3,712.2

deformation (Sousa et al. 2005; Kahraman et al. 2005; del Río et al. 2006; Cuccuru and Cherchi 2008). UCS testing shows the SG-Granite has an average strength of about 159 MPa, which is a high value for a weathered rock. When considering the results together, there is no obvious correlation between the microfracture density, degree of chemical weathering, and UCS (Fig. 3). Although the highest strength value is seen in the sample with the lowest CIA value and fracture density (004), it is apparent that most of the weathered samples (e.g., 040 and 001, CIA value of ~58 %) are more resistant than less weathered samples (e.g., 007 or 023, CIA value of ~56 %; Fig. 3). FS testing confirms this anomalous behaviour, as the lowest strength values (6.6 MPa) are found for samples with mid-range CIA and K values (Fig. 3).

Water absorption and capillarity rise cannot be obviously related to the microfracture system (Tables 3, 4); some samples with high K values show comparatively low absorption values (Tables 3, 5). Planar anisotropy, represented by microfracture arrays (C_1 and C_2), does not reflect any inconsistency in capillarity (Table 3).

In ultrasonic velocity tests on microfracture arrays, all samples had the lowest speeds at 90° to the trend of the microfracture (X_3) and higher speeds parallel to the microfracture system, (X_1 and X_2). Sample 004, which has the lowest K value, yielded a mean speed of 4,721 m/s and exhibits nearly isotropic behaviour.

Microfabric

K-feldspar and plagioclase are sub-idiomorphic and lack any clear SPO, in both XZ and YZ sections. Quartz forms irregularly shaped globules, weakly aligned parallel to the inferred magmatic flow direction (X). This general textural arrangement shows only minor changes between the periphery and the core of the granite sheet. The core, which represents the volumetrically significant part of the granitic body, contains quartz globules commonly enclosed by biotite flakes and feldspar-rich domains (Fig. 4). Boundaries between quartz globules and feldspars are straight or gently curved, although some microcline crystals have developed more irregular boundaries with cusps and lobes (Fig. 4). The orientation of both quartz–feldspar and feldspar–feldspar contacts is highly variable; i.e., boundaries do not match specific crystal facets. Within globules, quartz–quartz contacts are serrated in part, with straight segments oriented parallel to both rhomb and prismatic planes (Fig. 4). Quartz crystals are characterized internally by undulose extinction and large sub-grains with boundaries oriented parallel to either basal or prismatic planes. This sub-grain microstructure defines the typical 'chessboard pattern' frequently observed in suitably oriented crystals (Kruhl 1996). Four distinct maxima in quartz

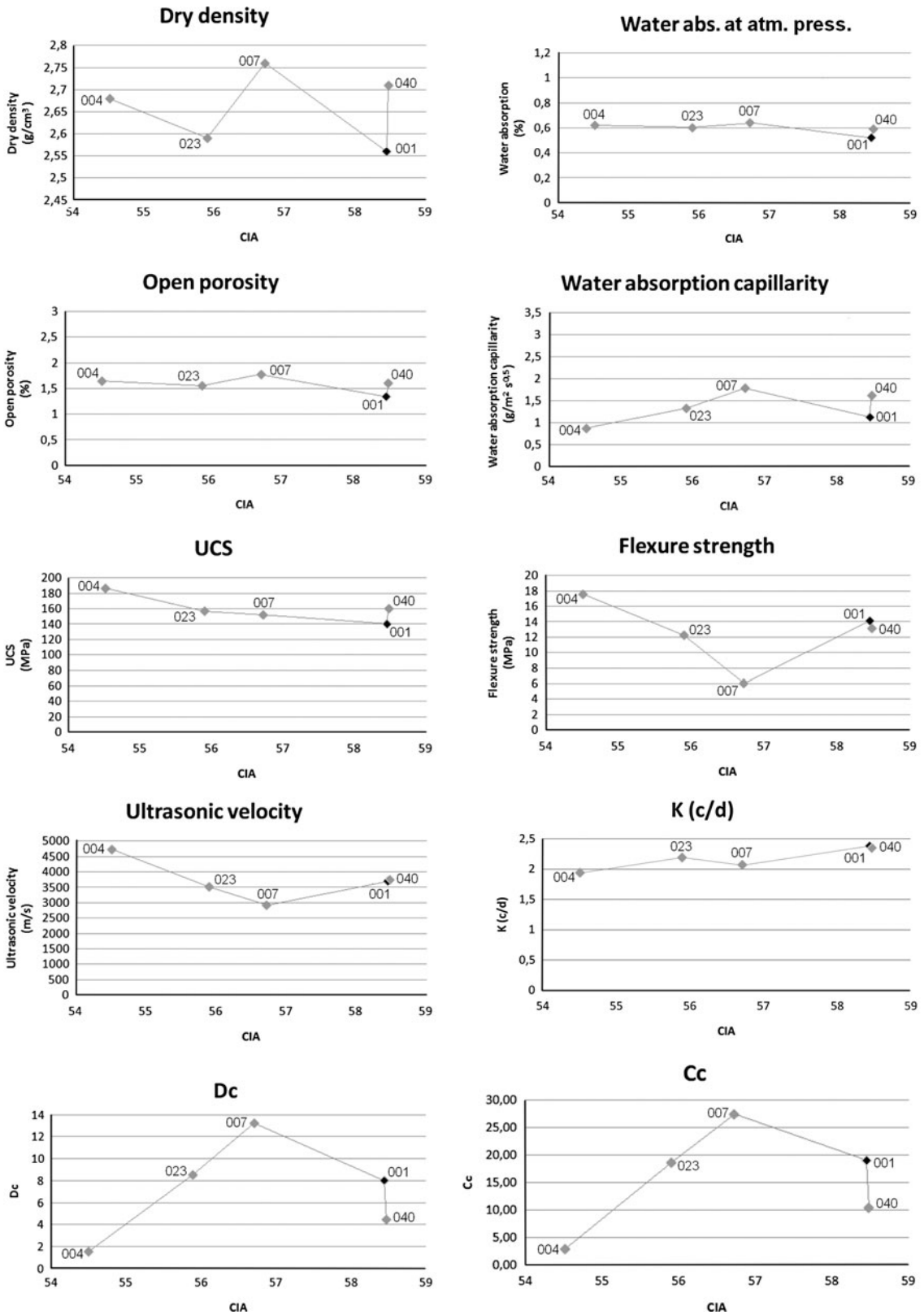

Fig. 3 Physical–mechanical properties, K, Dc and Cc versus the CIA index. *Black squares* represent the grey sample

Table 4 Correlation matrix (r value) between properties

	Dry density	Water abs. at atm. press.	Open porosity	Water abs. capillarity	UCS	Flexure strength	Ultrasonic velocity	CIA	Cc	Dc	K
Dry density		0.78	0.90	0.58	0.34	−0.47	−0.20	−0.13	0.04	0.12	−0.45
Water abs. at atm. press	0.78		0.97	0.34	0.57	−0.38	−0.09	−0.64	−0.01	0.11	−0.79
Open porosity	0.90	0.97		0.49	0.46	−0.49	−0.20	−0.46	0.08	0.19	−0.69
Water abs. capillarity	0.58	0.34	0.49		−0.47	−0.88	−0.85	0.47	0.66	0.67	0.25
UCS	0.34	0.57	0.46	−0.47		0.54	0.77	−0.77	−0.80	−0.73	−0.74
Flexure strength	−0.47	−0.38	−0.49	−0.88	0.54		0.94	−0.25	−0.89	−0.92	−0.03
Ultrasonic velocity	−0.20	−0.09	−0.20	−0.85	0.77	0.94		−0.46	−0.95	−0.94	−0.32
CIA	−0.13	−0.64	−0.46	0.47	−0.77	−0.25	−0.46		0.35	0.27	0.92
Cc	0.04	−0.01	0.08	0.66	−0.80	−0.89	−0.95	0.35		0.99	0.23
Dc	0.12	0.11	0.19	0.67	−0.73	−0.92	−0.94	0.27	0.99		0.12
K	−0.45	−0.79	−0.69	0.25	−0.74	−0.03	−0.32	0.92	0.23	0.12	

Table 5 Results of the fracture analysis with the linear intercept method: *Dc* linear fracture density, *Cc* linear fracture connectivity, *K* the ratio Cc/Dc

Sample	Dc	Cc	K
001	8.00	19.03	2.38
004	1.50	2.92	1.94
007	13.22	27.42	2.07
023	8.50	18.64	2.19
040	4.43	10.43	2.35

c-axis orientations (Fig. 4) define a strong lattice preferred orientation (LPO).

The load maxima (I and II) largely coincide with the inferred flow direction. The lighter maxima (III and IV) are on the XY plane, close to the Y direction. Microstructures in the peripheral facies (e.g., sample 004) are similar to those observed in the core. Large quartz crystals in this facies show consistent 'chessboard' microstructures, and the boundaries between quartz crystals with different lattice orientations are often sutured. In places, these boundaries also have discontinuous arrays of small, equi-axial grains (Fig. 4) of similar dimensions to adjacent sub-grains, and appear to have grown by dynamic re-crystallization (Hirth and Tullis 1992; Stipp et al. 2002). In these peripheral samples, quartz–quartz boundaries follow the rhomb and/or prismatic planes, whereas other phase boundaries (e.g., between different feldspars or between quartz and feldspar) have no preferred orientation. Quartz c-axis orientations (Fig. 4) are clustered in a load maximum (I) around the X direction, but other light maxima are present on the XY plane.

Microfractures

The microfracture network, when viewed in thin section, consists of two distinctive sets of cracks. First-order cracks (J1) form an array of highly pervasive, widely spaced fractures (mean spacing of about 0.5 mm) that cut through all minerals, though some small deviations are observed along sub-grain boundaries with favourable orientations (Fig. 5). J1 microfractures extend for several centimetres and are usually open, allowing the crack walls to split apart by 3–15 μm (Fig. 5). It is important to note that in more yellowish samples (e.g., 040) the fracture cavities can be partly or almost completely filled by fine-grained, idiomorphic Fe-oxides and hydroxides (Fig. 5). In some cases, J1 fractures also contain gouge, apparently derived from crushing of the crack walls (Fig. 5). In greyish samples (e.g., 001) Fe-oxides and hydroxides are virtually absent; thus, J1 fractures contain much less infill. In all samples, J1 fractures are associated with second-order J2 cracks (mean spacing ~0.05 mm; Fig. 5) that developed at the edges of, or within, quartz globules (Fig. 5). J2 cracks follow quartz–feldspar boundaries, quartz rhomb and prism sub-grain boundaries, and other rational crystal facets (Fig. 5). These microfractures disappear at the edges of quartz globules, but may bridge to J1 microfractures, enhancing the overall connectivity. J2 fractures are effectively crack–seal rather than discrete like J1 fractures; the distance between J2 crack walls is 0.05–0.5 μm in most cases.

Discussion

Effects of microstructure on fracture development

The microfracture network is the most distinctive structure observed in the SG-Granite. At first glance, it appears that J1 microfractures are not controlled by the SPO of rock-forming minerals, as neither feldspars nor biotite and quartz show any appreciable preferred orientation. This observation is confirmed by the fact that J1 fractures

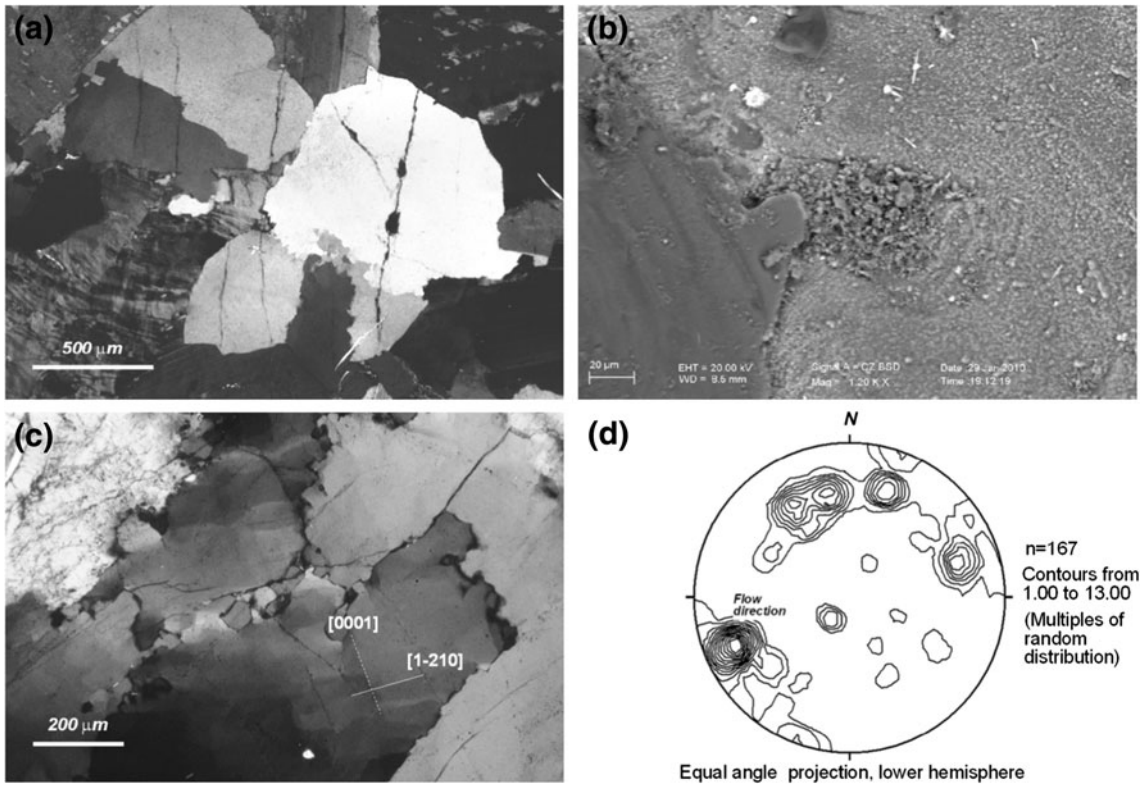

Fig. 4 Microstructure of the SG-Granite **a** polycrystalline quartz globule enclosed within microcline, plagioclase and biotite (photomicrograph, crossed polarizers), **b** SEM image of irregular phase-boundary contact between quartz (*left side*) and sericitized k-feldspar. Note the mirmekite in the *centre* of the image, developed against a large quartz edge, **c** 'chessboard' microstructure within quartz globules, both basal [0001] and prism [1-210] crystallographic planes are indicated (photomicrograph, crossed polarizers), **d** representative quartz c-axis fabric, the inferred direction of magmatic flow is indicated

remain consistently rectilinear, regardless of whether they pass through several different crystals of quartz and feldspar. On a smaller scale, crack walls take small deviations from the general trend and follow quartz–feldspar boundaries if the angle between the fracture and the boundary does not exceed 20°–30°.

In granitic rocks, micas trigger fracture development because of their low shear strength compared with both quartz and feldspar (Mares and Kronemberg 1993; Shea and Kronemberg 1993). Glide along the basal planes of suitably oriented mica crystals may, therefore, have had local effects on the geometry of J1 microfractures, as indicated by step-overs in corresponding biotite flakes. Although this is a positive feedback loop, the rarity of biotite throughout the SG-Granite indicates that regardless of the efficiency of this process, it has not significantly contributed to fracturing. However, deviations along otherwise straightforward J1 microfractures are common within larger quartz globules, giving a thunderbolt shape to the fracture trace in thin section. These sharp and short deflections are even more common in J2 microfractures.

Notably, deviations along microfractures commonly coincide with quartz rhomb and prism sub-grain boundaries; it seems likely that these specific lattice planes allowed the fractures to propagate. Both the quartz rhomb and prism sub-grain boundaries would behave as relatively weak planes under magmatic or sub-magmatic conditions (Gleason and Tullis 1995; Mainprice et al. 1993; Den Brok 1996). Most of these sub-grain boundaries contain trails of fluid inclusions, which could further contribute to lowering the effective strength of these microstructural sites. Given the strong quartz LPO throughout the granite sheet, it is suggested that the extensive highly connected system of microfractures resulted from a microstructural control exerted by a pre-existing, primary texture (Casini et al. 2008).

Microfractures, weathering, and rock toughness

The yellowish samples appear to be increasingly weathered with increasing intensity of their coloration. This speculation is logical at least to some extent; however, the CIA index shows small variations throughout all samples regardless of the intensity of the yellowish coloration. Therefore, two unrelated processes must be responsible for the chemical weathering and for the coloration.

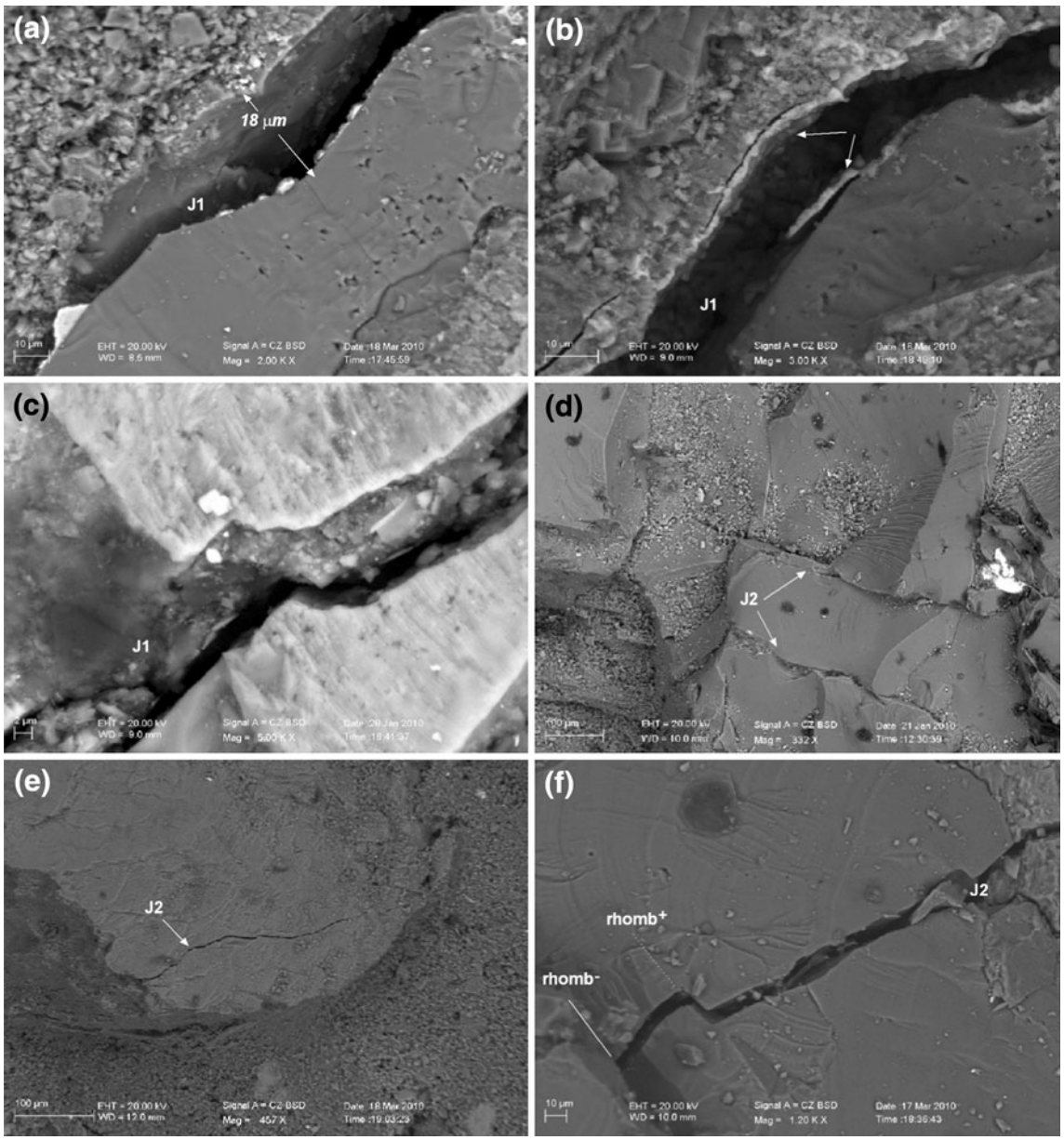

Fig. 5 SEM images of J1 microfractures (sample 040), broken surfaces, operating conditions are indicated on each image **a** the geometry of and the distance between the walls of a J1 microfracture, **b** close-up of the same fracture as in **a**, the *white arrows* indicate the film of Fe-oxides/hydroxides. Note that the separation between crack walls is an artifact due to sample preparation, **c** fine-grained gouge filling a J1 microfracture, **d** parallels J2 microfractures crossing through a quartz crystal, **e** extension of a J2 microfracture within a quartz globule, note that the fracture ends at the quartz–feldspar contacts, **f** geometry of a J2 microfracture, note the sharp deflection developed in correspondence of rhomb$^{+/-}$ subgrains

The extensive chemical weathering of feldspars observed throughout the SG-Granite was probably controlled by low-Eh hydrothermal fluids, which promoted the partial replacement of feldspars by patches of fine-grained white micas and quartz, and the chloritization of biotite. The coloration of the granite is apparently superficial, as after just a few months of exposure to air and rainfall, greyish blocks turn yellow. Based on these arguments, it is suggested that the coloration of the SG-Granite depends on the circulation of rainwater, which leads to the oxidization of biotite. Microstructural observations and SEM–EDX analyses indicate that staining of the SG-Granite results from precipitation in the microfractures of Fe-oxides/hydroxides derived from weathered biotite (Fig. 5). Apart from modifying the original greyish coloration, the precipitation of Fe-oxides/hydroxides seals the fractures, thus leading to the partial recovery of physical–mechanical properties in the granite. For example, sample 040, despite its highest CIA and K indices, shows a relative good toughness due to sealing of the fractures by Fe-oxides/hydroxides.

Table 6 Minor and trace elements composition. ICP MS (ppm)

	Samples	
	001	040
Sc	2	2
Be	1	1
V	<5	<5
Cr	30	40
Co	<1	<1
Ni	<20	<20
Cu	<10	<10
Zn	<30	<30
Ga	19	18
Ge	1	1
As	<5	<5
Rb	109	101
Sr	13	13
Y	29	29
Zr	223	269
Nb	8	6
Mo	3	4
Ag	<0.5	<0.5
In	<0.2	<0.2
Sn	2	4
Sb	<0.5	<0.5
Cs	1.3	1.1
Ba	191	189
La	32.8	32.6
Ce	72.2	73.5
Pr	7.75	7.82
Nd	27.8	27.7
Sm	5.5	5.3
Eu	0.21	0.21
Gd	4.8	4.7
Tb	0.7	0.7
Dy	3.9	3.7
Ho	0.7	0.7
Er	2.2	2.2
Tm	0.32	0.32
Yb	2.1	2.1
Lu	0.33	0.33
Hf	6.6	7.6
Ta	0.5	0.5
W	<1	<1
Tl	0.5	0.5
Pb	28	27
Bi	<0.4	<0.4
Th	15.3	15.1
U	2.3	2.6

These results indicate that staining and coloration are not useful indicators of alteration. In fact, there is no meaningful correlation between the intensity of the yellowish colour and the degree of chemical alteration; for example, sample 001 yielded a high CIA value despite its grey colour. Chemical alteration affects all sample sets and the yellowish coloration is due exclusively to the difference in iron oxidation state in the rock. Complete chemical analysis across the quarry log (Tables 2, 6) shows that compositional homogeneity is preserved from greyish to yellowish samples. It is likely that staining does not involve large-scale element mobilization, including iron, which has suffered complete oxidation and precipitation as Fe-oxides/hydroxides.

Conclusions

A thorough knowledge of a rock's physical–mechanical properties is essential when considering its suitability as a dimension stone (Sousa et al. 2005; Schöpfer et al. 2009). Commonly performed tests focus primarily on the macroscopic mechanical behaviour and neglect, almost entirely, microstructural anisotropies. Both fieldwork and preliminary laboratory tests on the SG-Granite have revealed that its toughness and unusual yellowish coloration reflect extensive near-surface weathering. Circulation of oxygen-rich rainwater within 5–10 m of the surface causes the oxidation of biotite, resulting in the yellowish coloration. Beyond the aesthetic result, this process gives renewed mechanical strength to the stone, allowing it to be used for structural, architectural and decorative purposes.

Acknowledgments This work was supported by Cofin 2008 grant (G. Oggiano) and Sardinia Government L.R. 7/2007—n° CRP2_104 grant (L. Casini and S. Cuccuru).

References

Aversano A (2003) Prospezione e caratterizzazione di rocce granitoidi della Sardegna Settentrionale: indicazioni in funzione dell'ottimizzazione del processo estrattivo e della mitigazione degli impatti. Ph.D Thesis, Università di Sassari

Carmignani L, Barca S, Disperati L, Fantozzi P, Funedda A, Oggiano G, Pasci S (1994) Tertiary compression and extension in the Sardinian basement. Boll Geofis Teor Appl 36:45–62

Casini L, Cuccuru S, Oggiano G, Cherchi GP (2008) Emplacement of the S. Giacomo pluton (North Sardinia, Italy) near the brittle-plastic transition: implications for the late Variscan deformation. Rendiconti online Società Geologica Italiana 3(1):186–187

Cherchi GP (2005) Prospezione e caratterizzazione di rocce granitoidi della Sardegna settentrionale: indicazioni per l'ottimizzazione del processo estrattivo e della mitigazione degli impatti. Ph.D Thesis, Università di Sassari

Cuccuru S, Cherchi GP (2008) Il Polo Estrattivo di Bassacutena: aspetti giacimentologici e caratterizzazione fisico-meccanica del granito "Rosa Beta". Rendiconti online Società Geologica Italiana 3(1):282–283

del Río LM, López F, Esteban FJ, Tejado JJ, Mota M, González I, San Emeterio JL, Ramos A (2006) Ultrasonic characterization of granites obtained from industrial quarries of Extremadura

(Spain). Ultrasonic 44:1057–1061. doi:10.1016/j.ultras.2006.05.098

Den Brok B (1996) The effect of crystallographic orientation on pressure solution in quartzite. J Struct Geol 18:859–860. doi:10.1016/s0191-8141(96)80018-6

Ferrè EC, Leake BE (2001) Geodynamic significance of early orogenic high-K crustal and mantle melts: example of the Corsica Batholith. Lithos 59:47–67. doi:10.1016/s0024-4937(01)00060-3

Gaggero L, Oggiano G, Buzzi L, Slejko F, Cortesogno L (2007) Post-Variscan mafic dykes from the late orogenic collapse to the Tethyan rift: evidence from Sardinia. Ofioliti 32:15–37

Gleason GC, Tullis J (1995) A flow law for dislocation creep of quartz aggregates determined with the molten salt cell. Tectonophysics 247:1–23. doi:10.1016/0040-1951(95)00011-b

Gupta AS, Seshagiri Rao K (2000) Weathering effects on the strength and deformational behavior of crystalline rocks under uniaxial compression state. Eng Geol 56:257–274

Hirth G, Tullis J (1992) Dislocation creep regimes in quartz aggregates. J Struct Geol 14:145–159

Kahraman S, Yeken T (2008) Determination of physical properties of carbonate rocks from P-wave velocity. Bull Eng Geol Environ 67:277–281. doi:10.1007/s10064-008-0139-0

Kahraman S, Gunaydin O, Fener M (2005) The effect of porosity on the relation between uniaxial compressive strength and point load index. Int J Rock Mech Min Sci 42:584–589. doi:10.1016/j.ijrmms.2005.02.004

Kruhl J (1996) Prism and basal-plane parallel boundaries in quartz: a microstructural geothermobarometer. J Struct Geol 14:581–589. doi:10.1046/j.1525-1314.1996.00413.x

Launeau P, Robin P-YF (1996) Fabric analysis using the intercept method. Tectonophysics 267:91–119. doi:10.1016/s0040-1951(96)00091-1

Mainprice D, Lloyd GE, Casey M (1993) Individual orientation measurements in quartz polycrystals: advantages and limitations for texture and petrophysical property determinations. J Struct Geol 15:1169–1187. doi:10.1016/0191-8141(93)90162-4

Mares VM, Kronemberg AK (1993) Experimental deformation of muscovite. J Struct Geol 15:1061–1075. doi:10.1016/0191-8141(93)90156-5

Matte P (2001) The Variscan collage and orogeny (480 ± 290 Ma) and the tectonic definition of the Armorica microplate: a review. Terra Nova 13:122–128. doi:10.1046/j.1365-3121.2001.00327.x

Nasseri MHB, Mohanty B, Robin P-YF (2005) Characterization of microstructures and fracture toughness in five granitic rocks. Int J Rock Mech Min Sci 42:450–460

Nesbitt HW, Young GM (1982) Early Proterozoic climates and plate motions inferred from major element chemistry of lutites. Nature 299:715–717

Oggiano G, Cherchi GP, Aversano A, Di Pisa A, Ulzega A, Orrù P, Pintus C (2005) Note illustrative della Carta Geologia d'Italia, Foglio 428 Arzachena. S.EL.CA, Firenze

Oggiano G, Funedda A, Carmigniani L, Pasci S (2009) The Sardinia–Corsica microplate and its role in the northern Apennine geodynamics: new insights from the tertiary intraplate strike-slip tectonics of Sardinia. Ital J Geosci 128(2):527–539. doi:10.3301/ijg.2010.26

Paquette JL, Ménot RP, Pin C, Orsini JB (2003) Episodic short-lived granitic pulses in a post-collisional setting: evidence from precise U–Pb zircon dating through a crustal cross-section in Corsica. Chem Geol 198:1–20. doi:10.1016/S0009-2541(02)00401-1

Paterson SR, Vernon RH, Tobish OT (1989) A review of criteria for the identification of magmatic and tectonic foliations in granitoids. J Struct Geol 2(3):349–363. doi:10-1016/0191-8141(89)90074-6

Schöpfer MPJ, Abe S, Childs C, Walsh JJ (2009) The impact of porosity and crack density on the elasticity, strength and friction of cohesive granular materials: insights from DEM modeling. Int J Rock Mech Min Sci 46:250–261. doi:10.1016/j.ijrmms.2008.03.009

Shea WT, Kronemberg AK (1993) Strength and anisotropy of foliated rocks with varied mica contents. J Struct Geol 15:1097–1121. doi:10.1016/0191-8141(93)90158-7

Sousa LMO, Suárez de Río LM, Calleja L, Ruiz de Aragoña VG, Rey AR (2005) Influence of microfractures and porosity on the physico-mechanical properties and weathering of ornamental granites. Eng Geol 77:153–168. doi:10.1016/j.enggeo.2004.10.001

Stipp M, Stüniz H, Heilbronner R, Schmid SM (2002) The eastern Tonale fault zone: a 'natural laboratory' for crystal plastic deformation of quartz over a temperature range from 250 to 700°C. J Struct Geol 24:1861–1884. doi:10.1016/s0191-8141(02)00035-4

UNI 9724/2 (1990) Materiali lapidei—determinazione della massa volumica apparente e del coefficiente d'imbibizione

UNI 9724/5 (1990) Materiali lapidei—determinazione della resistenza a flessione

UNI 9724/7 (1992) Materiali lapidei—determinazione della massa volumica reale e della porosità totale e accessibile

UNI EN 1925 (2000) Metodi di prova per pietre naturali—determinazione del coefficiente di assorbimento d'acqua per capillarità

UNI EN 1926 (2000) Metodi di prova per pietre naturali—determinazione della resistenza a compressione

UNI EN 13755 (2002) Metodi di prova per pietre naturali—determinazione dell'assorbimento d'acqua a pressione atmosferica